nature nanotechnology

ARTICLES

https://doi.org/10.1038/s41565-019-0527-6

Renal clearable catalytic gold nanoclusters for in vivo disease monitoring

Colleen N. Loynachan[1,10], Ava P. Soleimany[2,3,4,10], Jaideep S. Dudani[2,5], Yiyang Lin[1], Adrian Najer[1], Ahmet Bekdemir[2,4], Qu Chen[1], Sangeeta N. Bhatia[2,4,6,7,8,9*] and Molly M. Stevens[1*]

Ultrasmall gold nanoclusters (AuNCs) have emerged as agile probes for in vivo imaging, as they exhibit exceptional tumour accumulation and efficient renal clearance properties. However, their intrinsic catalytic activity, which can enable an increased detection sensitivity, has yet to be explored for in vivo sensing. By exploiting the peroxidase-mimicking activity of AuNCs and the precise nanometre-size filtration of the kidney, we designed multifunctional protease nanosensors that respond to disease microenvironments to produce a direct colorimetric urinary readout of the disease state in less than one hour. We monitored the catalytic activity of AuNCs in the collected urine of a mouse model of colorectal cancer in which tumour-bearing mice showed a 13-fold increase in colorimetric signal compared to healthy mice. The nanosensors were eliminated completely through hepatic and renal excretion within four weeks of injection with no evidence of toxicity. We envision that this modular approach will enable the rapid detection of a diverse range of diseases by exploiting their specific enzymatic signatures.

Democratization of diagnostic tools to enable the simple, sensitive and early detection of disease is essential, particularly in low- and middle-income countries, which bear a significant burden of both infectious and non-communicable diseases[1]. Although worldwide mortality rates due to infectious diseases have substantially decreased, the ever-increasing ageing population means cancer has become a primary cause of morbidity and mortality[2]. New globally accessible diagnostic tools will be key in addressing unmet challenges in global oncology. Advances in nanotechnology offer unprecedented solutions in the form of responsive detection tools that, when applied globally, can enable earlier diagnosis and better treatment irrespective of the local resources available[3].

Early diagnosis of cancer enables effective treatment of primary tumours via local therapeutic interventions, such as surgery and radiotherapy[4]. Early detection has largely relied on blood biomarkers. However, the prohibitively low rates at which most biomarkers are shed from tumours, the tremendous dilution in the circulation and the lack of specificity of secreted biomarkers impede early detection[5,6]. Protease activities are implicated in a wide range of non-communicable human diseases, which include cancer, inflammation and thrombosis. Monitoring protease activity as a biomarker of disease may be leveraged to overcome the lack of sensitivity and specificity of abundance-based blood biomarkers[7]. Common tools to measure protease activity often rely on cumbersome and infrastructure-heavy analyses, such as fluorescence[8–10], mass spectrometry[11] or magnetic resonance imaging[12]. Previously, we developed exogenously administered multiplexed protease-responsive nanoparticles that release small reporter probes into the urine in response to proteolytic cleavage in disease environments[3,13–15]. These protease nanosensors offer sensitivity advantages for in vivo protease monitoring due to the enzymatic amplification and renal concentration of reporter probes from the blood to urine, which allows for the direct measurement of reporters by mass spectrometry[16] or immunoassays[13,17]. In practice, however, these techniques require analysis and expensive analytical reagents not typically available in resource-limited settings. For precision medicine to become globally accessible, diagnostic tools that can probe protease activity with a simple and sensitive readout are required.

Ultrasmall (<2 nm) gold nanoclusters (AuNCs) offer an elegant solution to the need for simple and sensitive diagnostic readouts due to their discrete electronic and molecular-like properties[18,19]. Particularly, noble metal nanoclusters and nanoparticles can function as catalysts to disproportionate or decompose H_2O_2, which in turn can oxidize a chromogenic substrate to provide a colorimetric measure of catalytic activity, similar to the enzyme horseradish peroxidase[20–22]. Despite this potential to provide a high sensitivity and simple readout for early disease detection, to date AuNCs have been used in vivo solely for fluorescence and X-ray contrast bioimaging applications[23–25]. We therefore sought to leverage the catalytic activity of AuNCs to develop a nanosensor platform that produces a direct colorimetric readout of disease state.

Here, we present the design of a versatile and modular nanosensor that comprises renal clearable catalytic AuNCs tethered via peptide linkages to a larger protein carrier, which is disassembled in response to dysregulated protease activity at the site of disease. To demonstrate the modularity of the system in responding to different families of proteases, we synthesized functionalized peptide substrates shown to be specifically cleaved by either the serine protease thrombin [26,27] or the zinc-dependent matrix metalloproteinase 9 (MMP9), which play a critical role in cardiovascular disease or cancer, respectively[28,29]. We demonstrated the response of our

[1]Department of Materials, Department of Bioengineering, and Institute of Biomedical Engineering, Imperial College London, London, UK. [2]Koch Institute for Integrative Cancer Research, Massachusetts Institute of Technology, Cambridge, MA, USA. [3]Harvard Graduate Program in Biophysics, Harvard University, Boston, MA, USA. [4]Harvard-MIT Division of Health Sciences and Technology, Institute for Medical Engineering and Science, Massachusetts Institute of Technology, Cambridge, MA, USA. [5]Department of Biological Engineering, Massachusetts Institute of Technology, Cambridge, MA, USA. [6]Department of Electrical Engineering and Computer Science, Massachusetts Institute of Technology, Cambridge, MA, USA. [7]Department of Medicine, Brigham and Women's Hospital and Harvard Medical School, Boston, MA, USA. [8]Broad Institute of Massachusetts Institute of Technology and Harvard, Cambridge, MA, USA. [9]Howard Hughes Medical Institute, Cambridge, MA, USA. [10]These authors contributed equally: Colleen N. Loynachan, Ava P. Soleimany. *e-mail: sbhatia@mit.edu; m.stevens@imperial.ac.uk

protease nanosensors both in vitro and in vivo, which achieved sensitive disease detection with a rapid, colorimetric urinary readout in a mouse model of colorectal cancer using our MMP-responsive nanosensors. Our system exhibited a dual amplification platform: leveraging both the in vivo protease activity and the inorganic catalytic activity of AuNCs to provide a visual readout of the disease state directly in urine. With this method, we demonstrated that these AuNCs are small enough to be filtered efficiently through the kidneys and retain catalytic activity in cleared urine, and thus provide a versatile disease detection platform that is compatible for deployment at the point-of-care.

Peptide-templated catalytic AuNCs are stable in serum

Protease-responsive nanosensors were synthesized using biotinylated protease-cleavable peptides to template and stabilize the growth of catalytic AuNCs, which were further coupled to neutravidin (NAv). NAv was selected as a biocompatible carrier for protease-responsive AuNC reporter probes due to its high affinity for biotin and low non-specific binding properties (Fig. 1)[30]. The AuNC–NAv complex was then intravenously (i.v.) administered and specifically disassembled by proteases at the site of disease. Our system takes advantage of a biological pharmacokinetic switch, in which the size of the particle largely drives biodistribution[31,32]. Once proteolytically liberated from the NAv complex, AuNCs circulated via the bloodstream and were efficiently filtered into the urine through the kidneys due to their small size (<5 nm). A simple colorimetric assay was performed on the urine to assess the presence of AuNCs as an indicator of disease state (Fig. 1).

We used a co-templated approach to synthesize noble metal nanoclusters that incorporated both the tripeptide glutathione (GSH, γ-Glu–Cys–Gly), a common capping ligand in nanocluster synthesis[23,33], and a thiol-terminated functional protease-cleavable peptide (Table 1) that act as both stabilizing capping ligands and reducing agents for nanoparticle formation (Fig. 2a). Gold was selected as the core metal, as it exhibited the highest catalytic activity compared to platinum and gold–platinum bimetallic hybrid nanoclusters and could be produced with a low coefficient of variation (8.5%), an important consideration in designing a scalable diagnostic platform (Supplementary Fig. 1).

The peptide substrates used as templates for the AuNC synthesis were composed of three functional domains: an enzyme recognition motif, a C-terminal cysteine residue to provide a thiol group for sequestering Au ions and an N-terminal biotin ligand for an efficient conjugation to a NAv carrier protein. The advantage of this synthesis route to produce catalytic noble metal nanoclusters is the ability to incorporate responsive and functional ligands onto the surface through simple gold–thiol interactions in a one-pot synthesis. Additionally, we previously investigated carrier and linker-specific effects on cleavage rates[14], and hypothesized that the target protease may be sterically hindered from accessing the scissile bond when the peptide sequence is presented on the AuNC and simultaneously linked to the NAv core. To explore this hypothesis, we also synthesized longer peptides ($P1_{20}$ and $P2_{20}$) by incorporating glycine spacers between the N-terminus and protease recognition motif (Table 1). We assessed the ability of the relevant protease to cleave the peptide substrate by verifying the mass of fragments after in vitro protease degradation (Supplementary Fig. 2).

The AuNCs did not exhibit surface plasmon resonance, a characteristic of large gold nanoparticles, but rather exhibited molecular-like absorption and corresponding fluorescence properties, attributed to the discrete electronic state that arises from their size (Supplementary Fig. 3). Transmission electron microscope (TEM) images and size analysis of the peptide-templated AuNCs (Fig. 2b and Supplementary Figs. 4 and 5) showed that the average size (1.5 ± 0.4 nm (Fig. 2c)) was below the glomerular filtration cutoff (~5.5 nm), which makes them ideally suited for kidney clearance[31,32,34–36].

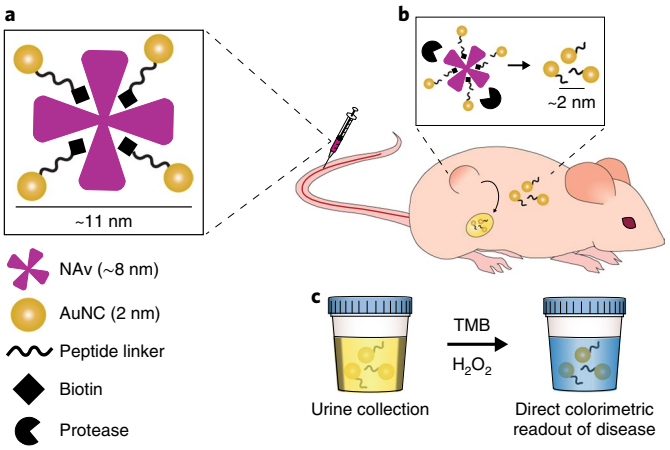

Fig. 1 | Design of the nanocatalyst signal amplification sensing system. **a**, Catalytic AuNCs were conjugated to a NAv protein scaffold through a biotinylated protease-cleavable peptide linker. **b**, The protease-sensitive AuNC–NAv complex (~11 nm) designed to specifically disassemble when exposed to the activity of the relevant dysregulated proteases at the site of disease was injected i.v. After protease cleavage (top), the liberated AuNCs (~2 nm) were filtered through the kidneys and into urine. **c**, The AuNCs were detected in the cleared urine by measuring their ability to oxidize a chromogenic peroxidase substrate (for example, TMB) in the presence of hydrogen peroxide and generate a coloured signal that can be easily read by eye.

The peroxidase-like catalytic activity of the AuNCs was measured using the oxidation of the peroxidase substrate 3,3′,5,5′-tetramethylbenzidine (TMB) by H_2O_2 as a model catalytic reaction, and absorbance at 652 nm (A_{652}) provided a colorimetric readout of the AuNC activity (Fig. 2d, Supplementary Figs. 1 and 6 and Supplementary Table 2). To assess the sensitivity of our catalytic reporter probes, we measured the catalytic activity of a dilution series of each AuNC batch in synthetic urine (Fig. 2e) and determined the limit of detection (LoD) to be ~2.7 pmol (25 µl of urine, ~100 nM AuNCs), with a broad linear response and dynamic range that spanned over three orders of magnitude of particle concentration.

There are several advantages to using inorganic AuNCs over natural peroxidases. Horseradish peroxidase is not feasible to use as a reporter probe in a comparable in vivo diagnostic system, as it is not readily cleared through the renal filtration pathway due to its size (~4.5 nm) and the tendency for proteins to be reabsorbed by the tubular epithelium[37]. Additionally, horseradish peroxidase is susceptible to non-specific degradation by endogenous proteases in vivo which would hinder the activity of any cleared enzyme[38]. However, AuNCs showed a high stability in physiological environments as they maintained catalytic activity, size and morphology in the presence of serum, urine and physiologically relevant glutathione concentrations (Fig. 2f and Supplementary Figs. 7–9). A key performance requirement of the AuNCs is that they retain their catalytic activity after exposure to complex environments, such as patient serum, which contains ~7 wt% protein. AuNCs effectively evaded non-specific protein adsorption and retained 80–90% of the catalytic activity after 1 h of incubation in fetal bovine serum (FBS, undiluted) or synthetic urine compared to PBS controls (Fig. 2f). In deciding which particle platform to take forward in vivo, we selected a system that balanced appropriate protease substrate loading with the retention of activity (Supplementary Fig. 10).

Renal clearance of AuNCs and activity retention in urine

The high physiological stability and retention of AuNC catalytic activity after exposure to serum and urine offered a unique opportunity

Table 1 | Protease-cleavable thiol-terminated peptide sequences for AuNC synthesis

Substrate	Protease specificity	Sequence[a]	MW (g/mol)	Product (g/mol)
$P1_{13}$	Thrombin	Biotin-SGG**fPR**↓SGGSGGC	1350	846
$P1_{20}$	Thrombin	Biotin-GGGSGGGSGG**fPR**↓SGGGGGC	1750	1275
$P2_{13}$	MMP9	Biotin-GGG**PLG**↓VRGKGGC	1339	683
$P2_{20}$	MMP9	Biotin-GGGGGGGGGG**PLG**↓VRGKGGC	1739	1080

Catalytic AuNCs were synthesized using GSH and another thiol-terminated protease-cleavable peptide sequence: $P1_{13}$, $P1_{20}$, $P2_{13}$ or $P2_{20}$, where the subscript indicates the number of amino acid residues in each sequence. AuNCs synthesized with the respective peptides were subsequently labelled AuNC–$P1_{13or20}$ and AuNC–$P2_{13or20}$. [a]↓, scissile bond; bold, enzyme recognition motif.

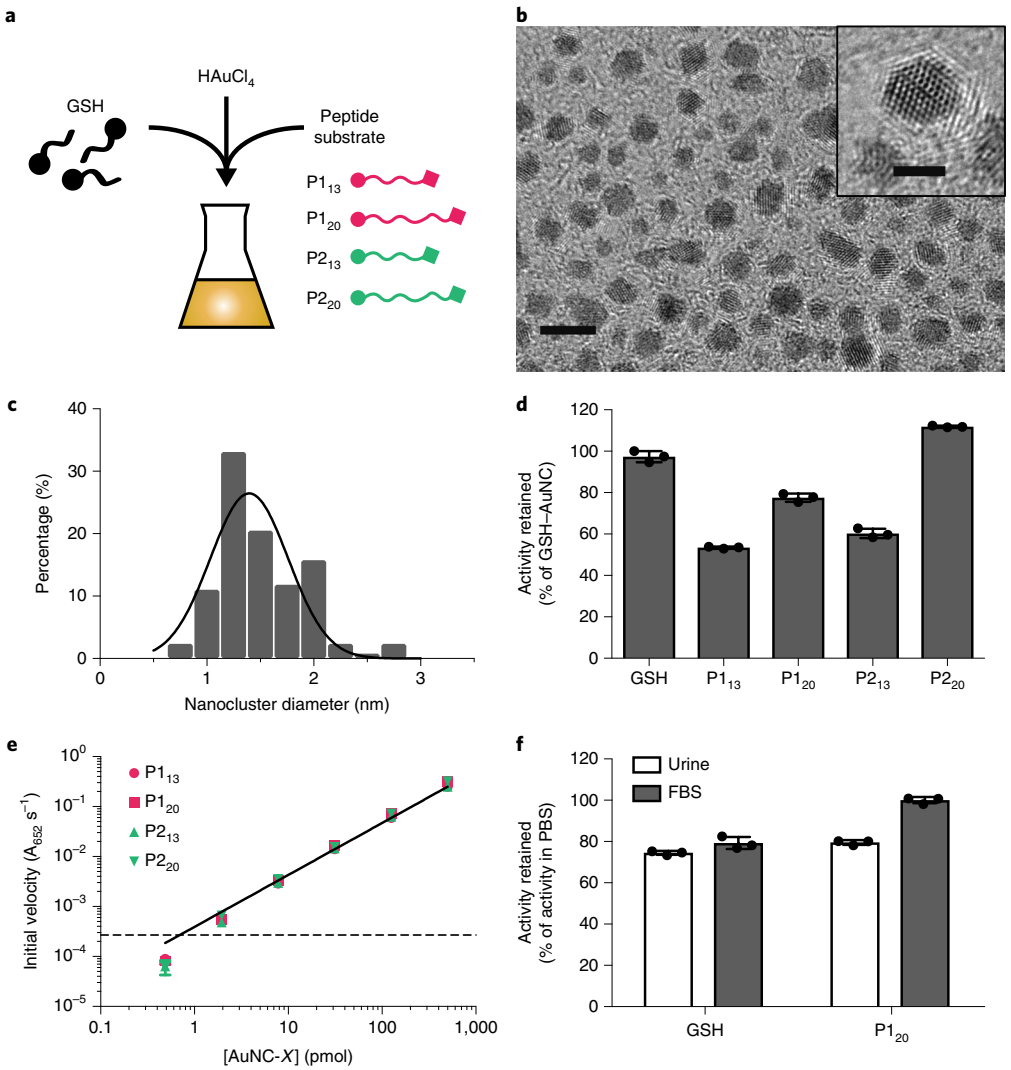

Fig. 2 | Peptide-functionalized AuNCs exhibit robust catalytic activity. a, The schematic shows the one-pot synthesis of AuNCs in which thiol-terminated heterobifunctional peptides ($P1_{13}$, $P1_{20}$, $P2_{13}$ and $P2_{20}$) were incorporated onto the AuNC surface. **b**, TEM image of GSH–AuNCs. Scale bar, 5 nm. Inset: high-resolution TEM of an individual GSH–AuNC. Scale bar, 2 nm. **c**, The histogram shows results of the size analysis from TEM images of GSH–AuNCs (mean diameter, 1.5 ± 0.4 nm (s.d.), $n = 127$ particles). The solid line represents a Gaussian fit of the size distribution. **d**, Catalytic activity of AuNCs capped with different cysteine-containing protease-cleavable peptide linkers (Table 1; mean ± s.d., $n = 3$ independent experiments). Activity was measured by A_{652}, which corresponds to the oxidation of the chromogenic peroxidase substrate TMB by H_2O_2 and normalized here to the activity of GSH–AuNCs in PBS. **e**, The LoD of reporter probes in synthetic urine measured by the catalytic activity of AuNCs functionalized with peptides, where $X = P1_{13or20}$ or $P2_{13or20}$ (mean ± s.d., $n = 3$ independent experiments). The catalytic activity was measured by the initial velocity analysis ($A_{652}\,s^{-1}$) of TMB oxidation. The solid line indicates that the activity for AuNCs is linear over three orders of magnitude of particle concentration with a non-linear (log scale) regression least-squares fit, $R^2 = 0.9996$. The dashed line represents the LoD, which was calculated as 3 standard deviations above the mean background signal. **f**, Catalytic activity of GSH–AuNCs and representative AuNC–$P1_{20}$ batch incubated in urine (undiluted) or serum (undiluted FBS) environments for 1 h. Activity was normalized to the activity of AuNCs in PBS (mean ± s.d., $n = 3$ independent experiments).

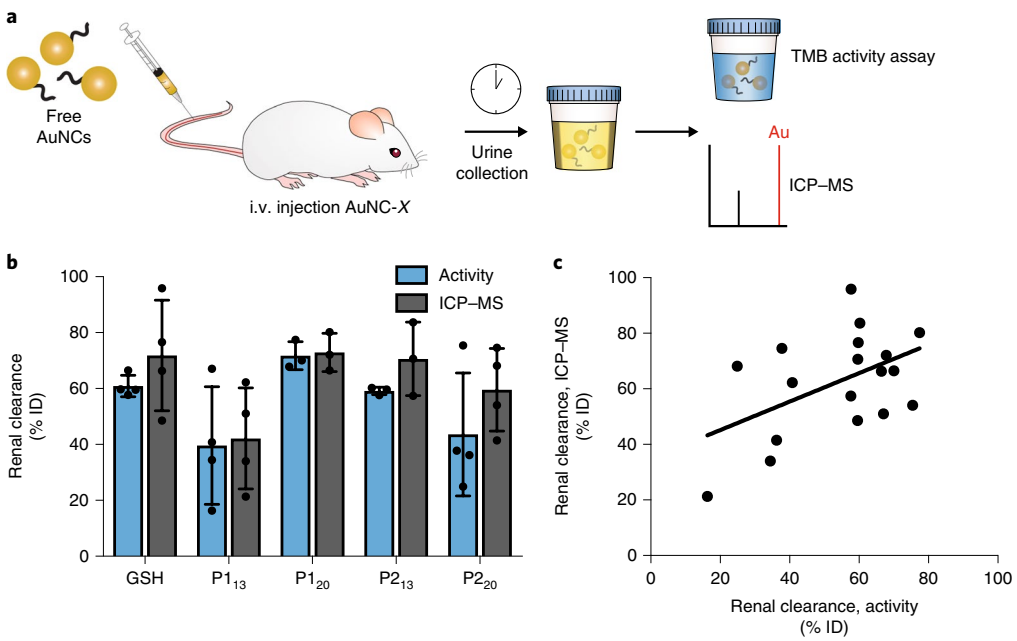

Fig. 3 | Peptide-functionalized AuNCs clear via the renal system and retain catalytic activity in urine. a, Schematic of the renal clearance assay. AuNCs were i.v. injected into Swiss Webster mice, and urine was collected 1 h p.i. Urine was analysed by both a TMB catalytic activity assay and ICP-MS to measure the gold content. **b**, Renal clearance efficiency of GSH-AuNC, AuNC-$P1_{13}$, AuNC-$P1_{20}$, AuNC-$P2_{13}$ and AuNC-$P2_{20}$ as measured by colorimetric assay (A_{652}) and by ICP-MS (estimated ppb cleared), normalized to activity and gold content, respectively, of the injected dose (mean ± s.d., $n = 3$ or 4 mice per group). **c**, Correlation between the estimated renal clearance as measured by colorimetric activity assay and by ICP-MS (Pearson's $r = 0.492$ with a 95% confidence interval (0.0320–0.780), $n = 18$ mice, $^*P = 0.0383$).

to non-invasively monitor AuNC clearance in urine by measuring the gold signal using both our catalytic activity assay and inductively coupled plasma–mass spectrometry (ICP–MS) (Fig. 3a). To determine the renal clearance efficiency, urine from mice injected with AuNCs was measured against a calibration curve for both catalytic activity and gold content. This showed that up to 73 ± 7% of the injected dose of functionalized AuNCs left the body via this route at 1 h postinjection (p.i.) and retained catalytic activity in urine (Fig. 3b). Encouragingly, the catalytic activity assay and ICP–MS results appeared to correlate (Fig. 3c, Pearson's $r = 0.492$, $^*P = 0.0383$). Thus, the catalytic activity assay can provide a simple and sensitive assessment of the presence of AuNCs in urine without the need for ICP–MS. Analysis of urine from mice injected with PBS revealed that no endogenous peroxidase activity was detectable in the collected urine (Supplementary Fig. 11). Using TEM image analysis, we confirmed that the size and morphology of the AuNCs cleared by the kidneys and excreted into the urine was comparable to those of the as-synthesized AuNCs (Supplementary Fig. 8). This indicates that the particle stability was unperturbed in vivo, which is consistent with the retention of the functional properties of the nanoclusters after in vivo interrogation.

AuNC nanosensors respond to protease activity in vitro

The biotin functional handles on the protease substrate-modified AuNCs were used to tether them to a NAv carrier protein to assemble an AuNC–NAv complex. Dynamic light scattering was used to monitor the size of the free AuNCs, NAv carrier and assembled AuNC–NAv complex (Supplementary Figs. 12 and 13), with representative hydrodynamic diameters of 2.5 ± 0.6 nm (glutathione-protected AuNC, GSH–AuNC), 3.3 ± 0.7 nm (AuNC–$P1_{20}$), 7.9 ± 1.5 nm (NAv) and 11.3 ± 2.2 nm (AuNC–$P1_{20}$–NAv).

To explore the kinetics of the proteolytic cleavage of the AuNC–NAv complexes, we employed fluorescence correlation spectroscopy (FCS) as a single-molecule detection method (Fig. 4a). After enzyme incubation, the diffusivity of the complex shifted over time towards that of the free fluorescently labelled clusters, which indicated that cleavage had occurred (Fig. 4b). Hydrodynamic size analysis by FCS showed that the MMP-responsive AuNC–$P2_{20}$–NAv complex was completely disassembled within 4.5 h of MMP9 incubation (Fig. 4c). The size of the thrombin-cleavable complex, AuNC–$P1_{20}$–NAv, did not significantly change when incubated with MMP9, and the size of the MMP-responsive AuNC–$P2_{20}$–NAv complex did not fall below the renal filtration limit when incubated with an off-target enzyme, in this case thrombin, for 12 h. Taken together, these results show the specificity of our nanosensors for their target enzymes. To demonstrate the modularity of our system, we used FCS to measure the disassembly kinetics of the thrombin-responsive complex (AuNC–$P1_{20}$–NAv), which was efficiently cleaved by thrombin (Supplementary Fig. 14). Further, MMP9 exhibited a rate of 3% AuNCs cleaved per minute towards the AuNC–$P2_{20}$–NAv complex, whereas the rate was only 0.08% AuNCs cleaved per minute towards the AuNC–$P2_{13}$–NAv complex (Fig. 4d). This ~40-fold increase in the cleavage rate for the complex formed with the longer linker could be attributed to the increased accessibility of the enzyme to the scissile bond. FCS results showed that in the presence of biologically relevant enzyme concentrations[39], significant cleavage was observed for AuNC–$P2_{20}$–NAv complexes, with 80% of the AuNCs cleaved within the first hour of incubation with MMP9.

Proteolytic cleavage of the AuNC–NAv complexes was further characterized in vitro by incubating complexes with recombinant protease, using gel filtration chromatography (GFC) to separate the cleavage products by size and monitoring the cleavage with a catalytic activity assay (Fig. 4e,f and Supplementary Fig. 13). The extent of the cleavage of the AuNC–NAv complex under different conditions was quantified by analysing the area under the curve associated with each cleavage product from the activity assay (Supplementary Table 3). Non-specific cleavage was investigated

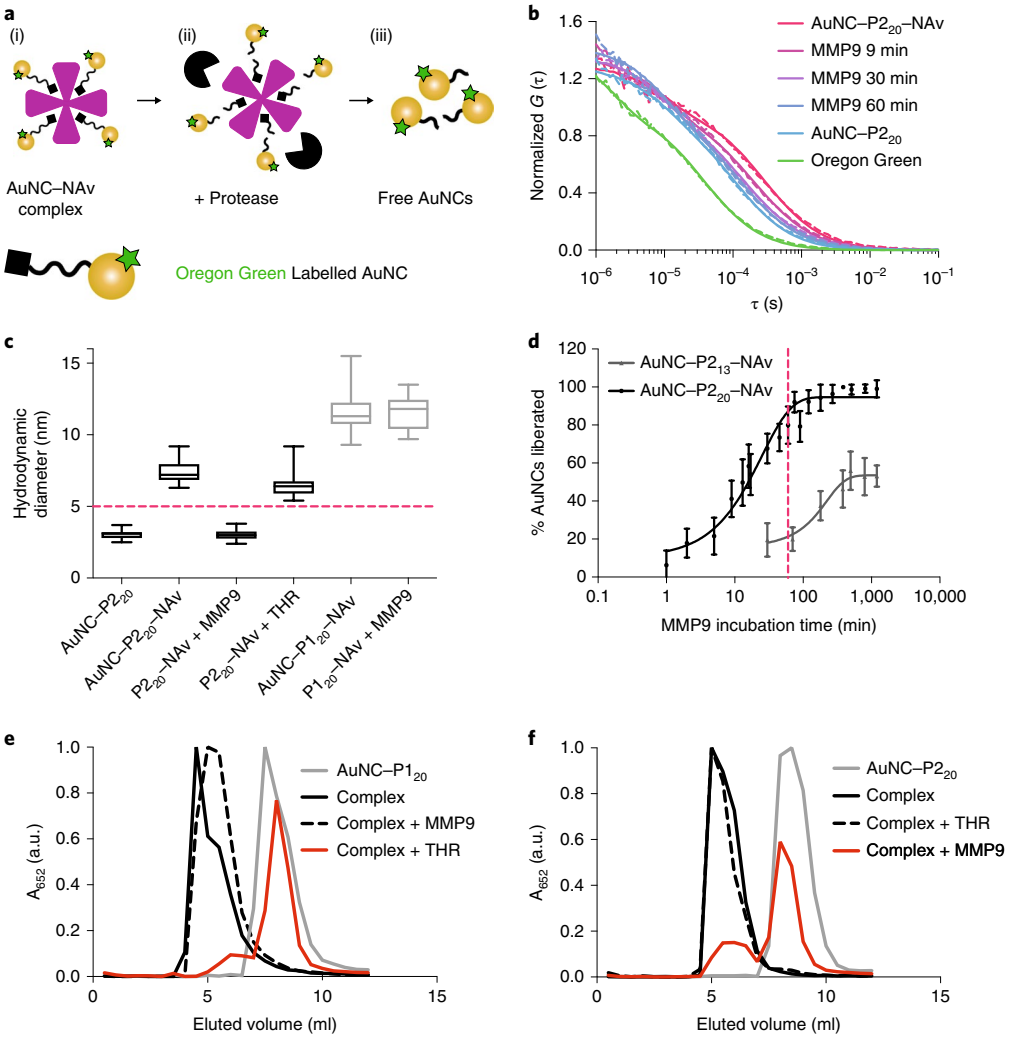

Fig. 4 | AuNC–NAv complexes disassemble in vitro in response to protease activity. a, Schematic illustration of FCS experiment. (i) AuNCs were labelled with a fluorescent dye and complexed to a NAv core; (ii) Dye-labelled AuNC–NAv complexes were incubated with the relevant enzyme, MMP9 or thrombin; and (iii) FCS was used to monitor the changes in diffusion time due to enzyme cleavage. **b**, Average autocorrelation curves from FCS measurements ($n = 25$ independent measurements) show the AuNC–P2$_{20}$–NAv complex in the presence of MMP9 (50 nM) over time compared to free labelled AuNCs and Oregon Green dye (dashed lines, experimental; solid lines, fits). A clear shift to faster diffusion times was observed for longer enzyme incubation times (red to blue colour change), which indicates cleavage of AuNCs from the complex. **c**, Hydrodynamic diameters calculated from the FCS autocorrelation curves show changes in the sizes of the complexes after enzyme incubation: AuNC–P2$_{20}$–NAv + MMP9 (50 nM, 4.5 h) or thrombin (THR) (50 nM, 12 h); AuNC–P1$_{20}$–NAv + MMP9 (50 nM, 12 h). The dashed line represents the renal filtration size cutoff of ~5 nm (ref. [32]). Centre line, the median; box limits, upper and lower quartiles; whiskers, minimum and maximum values ($n = 25$ independent measurements). **d**, Plot of fraction of AuNCs liberated (Supplementary Information) from the AuNC–P2$_{13or20}$–NAv complex for MMP-responsive complexes composed of either short or long linkers incubated with MMP9 (50 nM) up to 16 h (mean ± s.d., $n = 25$ independent measurements). The dashed line at 60 min corresponds to time frame of the in vivo experiments. **e**, Normalized absorbance showing the catalytic activity of GFC column fractions associated with AuNC–P1$_{20}$, the thrombin-responsive AuNC–P1$_{20}$–NAv complex (Complex), AuNC–P1$_{20}$–NAv (10 μM) incubated with MMP9 (50 nM, 12 h) (Complex + MMP9), and AuNC–P1$_{20}$–NAv complex (10 μM) incubated with thrombin (50 nM, 12 h) (Complex + THR). **f**, Normalized absorbance showing the catalytic activity of GFC column fractions associated with AuNC–P2$_{20}$, MMP-responsive AuNC–P2$_{20}$–NAv complex (Complex), the AuNC–P2$_{20}$–NAv complex (10 μM) incubated with thrombin (50 nM, 12 h) (Complex + THR) and the AuNC–P2$_{20}$–NAv (10 μM) incubated with MMP9 (50 nM, 12 h) (Complex + MMP9). All the enzyme incubations were performed at 37 °C, and all the GFC experiments were repeated independently three times with similar results.

by incubating AuNC–P1$_{20}$–NAv with MMP9 and AuNC–P2$_{20}$–NAv with thrombin. A low background cleavage by the off-target enzyme was observed (Fig. 4e,f), in agreement with FCS results. Finally, we explored the sensitivity of our nanosensor to MMP9 activity in vitro using both FCS and a filtration-based colorimetric catalytic activity assay (Supplementary Fig. 15), and low nanomolar sensitivities were observed, comparable to those of commercial in vitro fluorogenic protease activity assays.

Biodistribution and clearance pathways for nanosensors

We assessed the biocompatibility of the AuNC–NAv complexes in vitro and found that they were non-toxic to HEK293T cells up to 15 μM (Supplementary Fig. 16). The toxicological responses of our AuNC–NAv complexes (3,000 pmol AuNC dose) in vivo were investigated by examining the pathology of the mice after the complex injection. No significant changes in bodyweight over 28 days and no histological evidence of heart, lung, liver, spleen or kidney

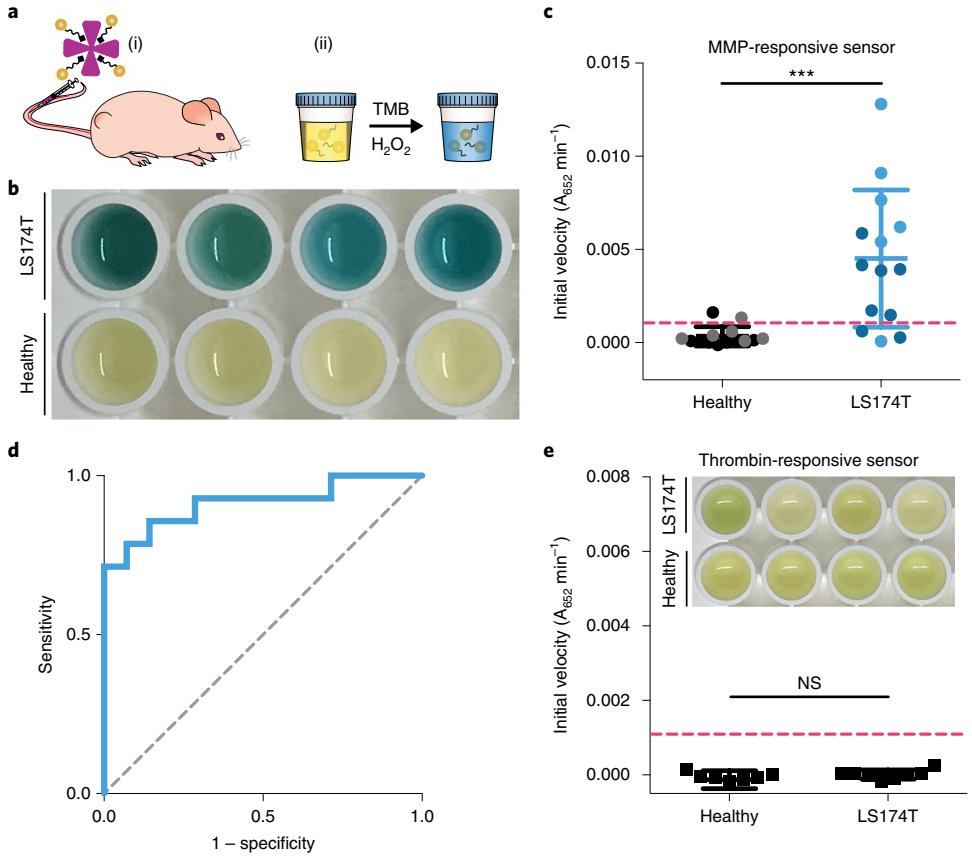

Fig. 5 | AuNC-functionalized protease nanosensors enable a direct colorimetric urinary readout of the disease state. a, (i) Mice that bore LS174T flank xenografts (2 weeks post-inoculation) and age-matched healthy controls were injected i.v. with the AuNC-$P2_{20}$-NAv complex. (ii) Urine was collected 1 h p.i. and the renal clearance of liberated AuNCs was measured by catalytic activity assay. **b**, Photograph of representative examples of the colorimetric assay on urine from tumour-bearing (top) and healthy (bottom) mice injected with AuNC-$P2_{20}$-NAv ($n = 4$ mice per group shown). **c**, Catalytic activity assay on urine collected from healthy and LS174T tumour-bearing mice 1 h p.i. with the AuNC-$P2_{20}$-NAv complex (mean ± s.d., $N = 2$ independent experiments indicated in shades, $n = 6$ (grey and light blue) or 8 (black and dark blue) mice per group, two-tailed Mann–Whitney test, $^{***}P = 0.0002$). The catalytic activity was measured by initial velocity analysis (A_{652} min^{-1}), and the dashed line represents the LoD (Methods). **d**, Receiver operating characteristic curve by the initial velocity of the catalytic activity assay discriminated healthy from diseased mice with an area under the curve of 0.91 ($N = 2$ independent experiments, $n = 6$ or 8 mice per group as in **c**, $P = 0.0002$ from a random classifier shown by the dashed line). **e**, Catalytic activity assay on urine from healthy and tumour-bearing mice injected with thrombin-responsive AuNC-$P1_{20}$-NAv complex. Inset: photograph of representative examples. No visible colorimetric development was observed in either group, and there was no statistically significant difference between the two groups (mean ± s.d., $n = 8$ mice per group, two-tailed Mann–Whitney test, $P = 0.161$, NS, not significant). The catalytic activity was measured by initial velocity analysis (A_{652} min^{-1}), and the dashed line represents the LoD (Methods).

toxicity were found at both short (1 h) and longer (24 h and 10 days) time points p.i., which suggests that AuNC–NAv complexes did not induce significant systemic toxicity (Supplementary Fig. 16).

To assess the clearance time frames and mechanisms, we explored the organ biodistribution, blood pharmacokinetics, urine composition and elimination pathways of AuNCs and AuNC–NAv complexes labelled with a photostable near-infrared dye. From the organ biodistribution study, free AuNCs accumulated most significantly in the kidneys relative to other organs, including the liver, at 1 h p.i. and were completely cleared from all major organs within seven days p.i. To corroborate the biodistribution study, we measured the gold signal in the urine by ICP–MS and our catalytic activity assay, and the presence of AuNCs was undetectable 24 h p.i. (Supplementary Fig. 17 and Supplementary Table 4). Owing to their size (~11 nm), the intact AuNC–NAv complexes accumulated predominately in the reticuloendothelial system organs[40]. The AuNC–NAv signal in the liver increased up to 24 h p.i., significantly decreased after 1 week, and was completely undetectable in all major organs 4 weeks p.i. (Supplementary Fig. 18). Encouragingly, the biodistribution and histology results suggest that, in healthy animals, intact AuNC–NAv complexes were cleared from the circulation and taken up in reticuloendothelial system organs and eliminated completely through hepatic (bile to faeces) and renal (urine) excretion within 4 weeks p.i. with no evidence of systemic or tissue-level toxicity.

Disease detection through colour change in urine

After confirming the successful cleavage by recombinant proteases in vitro, we sought to apply the protease-responsive AuNC nanosensor platform to in vivo disease detection using the colorimetric urinary readout. We characterized the pharmacokinetics of the NAv carrier, AuNC–NAv complex and free AuNCs in terms of accumulation in organs and tumour xenografts of the human colorectal cancer cell line LS174T, which secretes MMP9[13] (Supplementary Fig. 19). Based on the measured blood half-life of the AuNC–NAv complex and the degree of tumour accumulation within 1 h p.i., we selected 1 h after nanosensor injection as our time point for urine collection.

For in vivo tumour detection experiments, tumour-bearing and healthy control mice were i.v. injected with MMP-responsive AuNC–$P2_{20}$–NAv nanosensors (Fig. 5a). Urine was collected from mice 1 h p.i., and the catalytic activity assay was run using 25 µl of urine sample. Comparing the signals from the healthy and tumour-bearing mice, we observed a blue colour that could be read by eye in the urine samples from tumour-bearing mice after the addition of the chromogenic peroxidase substrate TMB (Fig. 5b). Quantification revealed a mean urinary signal increase of approximately 13-fold in the tumour-bearing mice relative to the healthy mice, as measured by the direct colorimetric readout and initial velocity analysis ($A_{652}\,min^{-1}$) of cleared AuNC catalytic activity in the collected urine (Fig. 5c). The AuNC catalytic activity measured corresponded to ~3.2% of the injected dose in urine from the tumour-bearing mice compared to a 0.2% renal clearance in the healthy mice, normalized using urine volumes (Supplementary Fig. 20). We believe our platform might benefit from improved diffusion, transport, tumour accumulation and clearance properties of peptide-templated AuNCs compared to larger nanomaterials commonly used in delivery applications, for which only ~0.7% of the administered nanoparticle dose was reported to be delivered to the solid tumour[41–43]. Receiver operating characteristic analysis revealed that the colorimetric test was highly accurate and discriminated the presence of colorectal cancer xenografts with an area under the curve of 0.91 (Fig. 5d, $P = 0.0002$). Furthermore, the delivery of our nanosensors to malignant tissues can be enhanced by exploiting our one-pot synthesis scheme for the incorporation of active targeting ligands, for example, the integrin-targeting ligand iRGD[14], onto the surface of the AuNCs.

Having established that the MMP-responsive AuNC nanosensors could discriminate between tumour-bearing and healthy mice, we sought to assess whether the urinary signal was driven by disease-associated protease activity. There was no significant difference in urine volumes between the groups, and analysis of the urine samples from PBS-injected healthy and tumour-bearing mice confirmed that no endogenous peroxidase activity was present in the absence of the injected nanosensors (Supplementary Fig. 20). TEM image analysis of the urine from tumour-bearing mice confirmed the presence of AuNCs cleared by the kidney, with size and morphology comparable to the as-synthesized AuNCs (Supplementary Fig. 8c). To ensure that the AuNC–NAv complex was not disassembling in vivo due to poor chemical stability or non-specific cleavage, we tested a substrate that we did not expect to be specifically cleaved in the tumour model[17]. Thrombin-responsive AuNC–$P1_{20}$–NAv complexes were injected into tumour-bearing and healthy mice and did not result in any significant colorimetric signal in the urine from the tumour-bearing mice compared to healthy controls (Fig. 5e). This pattern suggested that there is a non-promiscuous release of AuNCs in vivo from AuNC–$P2_{20}$–NAv complexes that is amplified in tumour-bearing mice, where elevated MMP levels at the site of disease and in circulation may actively disassemble AuNC–NAv complexes. Taken together, these results demonstrate that the AuNC–NAv nanosensors respond to disease-specific proteolytic activity in vivo and enable a direct colorimetric readout of the disease state, as evidenced by highly accurate discrimination in a flank tumour model of human colorectal cancer.

Conclusions

We have developed a modular approach for the rapid detection of a disease state based on a simple and sensitive colorimetric urinary assay that requires minimal equipment and can be read by eye in less than one hour. We synthesized ~2 nm catalytic AuNC probes modified with orthogonal protease substrates that are responsive to multiple enzymes. We demonstrated that the peptide-templated AuNCs can be filtered through the kidneys and excreted into the urine with high efficiency and that they retain their catalytic activity in complex physiological environments. We assembled the AuNC probes into larger complexes, which were disassembled in vitro in response to specific proteases. Finally, we deployed MMP-responsive AuNC–NAv complexes in vivo in a colorectal cancer mouse model and successfully detected AuNCs in urine from tumour-bearing mice with a facile colorimetric readout.

Here we show that, through the rational surface modification of AuNCs, we can engineer nanosensors that can be deployed in vivo and exploit the intrinsic catalytic activity of renal clearable noble metal nanoclusters as a disease indicator. We present a versatile toolbox that can be used to probe the complex enzymatic profiles of specific disease microenvironments, the results of which will open new opportunities to develop translatable responsive and catalytic nanomaterial diagnostics for a range of diseases in which enzyme activity can be used as a biomarker. We envision that clinical application of this technology may additionally take advantage of multiplexed protease substrate linkages, such as those responsive to Boolean logic operations[44,45], which may be able to profile the activities of proteases of diverse classes to distinguish between cancers and other pathologies. Our adaptable nanocatalyst amplification platform should be applicable in low-resource settings for the rapid detection of a diverse range of disease-associated proteases, which include those implicated in infectious diseases, and will democratize access to advanced and sensitive diagnostics.

Online content

Any methods, additional references, Nature Research reporting summaries, source data, statements of code and data availability and associated accession codes are available at https://doi.org/10.1038/s41565-019-0527-6.

Received: 13 November 2018; Accepted: 16 July 2019;
Published online: 02 September 2019

References

1. *Global Action Plan for the Prevention and Control of Noncommunicable Diseases 2013–2020* (World Health Organization, 2013).
2. Selmouni, F. et al. Tackling cancer burden in low-income and middle-income countries: Morocco as an exemplar. *Lancet Oncol.* **19**, e93–e101 (2018).
3. Kwon, E. J., Lo, J. H. & Bhatia, S. N. Smart nanosystems: bio-inspired technologies that interact with the host environment. *Proc. Natl Acad. Sci. USA* **112**, 14460–14466 (2015).
4. Etzioni, R. et al. The case for early detection. *Nat. Rev. Cancer* **3**, 235 (2003).
5. Hori, S. S. & Gambhir, S. S. Mathematical model identifies blood biomarker-based early cancer detection strategies and limitations. *Sci. Transl. Med.* **3**, 109ra116 (2011).
6. Henry, N. L. & Hayes, D. F. Cancer biomarkers. *Mol. Oncol.* **6**, 140–146 (2012).
7. Lopez-Otin, C. & Bond, J. S. Proteases: multifunctional enzymes in life and disease. *J. Biol. Chem.* **283**, 30433–30437 (2008).
8. Hilderbrand, S. A. & Weissleder, R. Near-infrared fluorescence: application to in vivo molecular imaging. *Curr. Opin. Chem. Biol.* **14**, 71–79 (2010).
9. Whitney, M. et al. Ratiometric activatable cell-penetrating peptides provide rapid in vivo readout of thrombin activation. *Angew. Chem. Int. Ed.* **52**, 325–330 (2013).
10. Whitley, M. J. A mouse-human phase 1 co-clinical trial of a protease-activated fluorescent probe for imaging cancer. *Sci. Transl. Med.* **8**, 320ra4 (2016).
11. Yepes, D. et al. Multiplex profiling of tumor-associated proteolytic activity in serum of colorectal cancer patients. *Proteom. Clin. Appl.* **8**, 308–316 (2014).
12. Choi, J. S. et al. Distance-dependent magnetic resonance tuning as a versatile MRI sensing platform for biological targets. *Nat. Mater.* **16**, 537–542 (2017).
13. Warren, A. D., Kwong, G. A., Wood, D. K., Lin, K. Y. & Bhatia, S. N. Point-of-care diagnostics for noncommunicable diseases using synthetic urinary biomarkers and paper microfluidics. *Proc. Natl Acad. Sci. USA* **111**, 3671–3676 (2014).
14. Kwon, E. J., Dudani, J. S. & Bhatia, S. N. Ultrasensitive tumour-penetrating nanosensors of protease activity. *Nat. Biomed. Eng.* **1**, 0054 (2017).
15. Schuerle, S., Dudani, J. S., Christiansen, M. G., Anikeeva, P. & Bhatia, S. N. Magnetically actuated protease sensors for in vivo tumor profiling. *Nano Lett.* **16**, 6303–6310 (2016).
16. Kwong, G. A. et al. Mass-encoded synthetic biomarkers for multiplexed urinary monitoring of disease. *Nat. Biotechnol.* **31**, 63–70 (2013).

17. Dudani, J. S., Buss, C. G., Akana, R. T. K., Kwong, G. A. & Bhatia, S. N. Sustained-release synthetic biomarkers for monitoring thrombosis and inflammation using point-of-care compatible readouts. *Adv. Funct. Mater.* **26**, 2919–2928 (2016).
18. Jin, R. Quantum sized, thiolate-protected gold nanoclusters. *Nanoscale* **2**, 343–362 (2010).
19. Jin, R., Zeng, C., Zhou, M. & Chen, Y. Atomically precise colloidal metal nanoclusters and nanoparticles: fundamentals and opportunities. *Chem. Rev.* **116**, 10346–10413 (2016).
20. Xia, X. et al. Pd–Ir core–shell nanocubes: a type of highly efficient and versatile peroxidase mimic. *ACS Nano* **9**, 9994–10004 (2015).
21. Loynachan, C. N. et al. Platinum nanocatalyst amplification: redefining the gold standard for lateral flow immunoassays with ultrabroad dynamic range. *ACS Nano* **12**, 279–288 (2018).
22. Tao, Y., Li, M., Ren, J. & Qu, X. Metal nanoclusters: novel probes for diagnostic and therapeutic applications. *Chem. Soc. Rev.* **44**, 8636–8663 (2015).
23. Zhang, X.-D. et al. Ultrasmall glutathione-protected gold nanoclusters as next generation radiotherapy sensitizers with high tumor uptake and high renal clearance. *Sci. Rep.* **5**, 8669 (2015).
24. Chen, Y. et al. Shortwave infrared in vivo imaging with gold nanoclusters. *Nano Lett.* **17**, 6330–6334 (2017).
25. Yang, W., Guo, W., Chang, J. & Zhang, B. Protein/peptide-templated biomimetic synthesis of inorganic nanoparticles for biomedical applications. *J. Mater. Chem. B* **5**, 401–417 (2017).
26. Davie, E. W. & Kulman, J. D. An overview of the structure and function of thrombin. *Semin. Thromb. Hemost.* **32**, 3–15 (2006).
27. ten Cate, H. & Hemker, H. C. Thrombin generation and atherothrombosis: what does the evidence indicate? *J. Am. Heart Assoc.* **5**, 1–8 (2016).
28. Roy, R., Yang, J. & Moses, M. A. Matrix metalloproteinases as novel biomarkers and potential therapeutic targets in human cancer. *J. Clin. Oncol.* **27**, 5287–5297 (2009).
29. Dudani, J. S., Warren, A. D. & Bhatia, S. N. Harnessing protease activity to improve cancer care. *Annu. Rev. Cancer Biol.* **2**, 53–76 (2018).
30. Jain, A., Barve, A., Zhao, Z., Jin, W. & Cheng, K. Comparison of avidin, neutravidin, and streptavidin as nanocarriers for efficient siRNA delivery. *Mol. Pharm.* **14**, 1517–1527 (2017).
31. Soo Choi, H. et al. Renal clearance of quantum dots. *Nat. Biotechnol.* **25**, 1165–1170 (2007).
32. Du, B., Yu, M. & Zheng, J. Transport and interactions of nanoparticles in the kidneys. *Nat. Rev. Mater.* **3**, 358–374 (2018).
33. Luo, Z. et al. From aggregation-induced emission of Au(I)–thiolate complexes to ultrabright Au(0)@Au(I)–thiolate core–shell nanoclusters. *J. Am. Chem. Soc.* **134**, 16662–16670 (2012).
34. Yu, M. et al. Noninvasive staging of kidney dysfunction enabled by renal-clearable luminescent gold nanoparticles. *Angew. Chem. Int. Ed.* 55, 2787–2791 (2016).
35. Ning, X. et al. Physiological stability and renal clearance of ultrasmall zwitterionic gold nanoparticles: ligand length matters. *APL Mater* **5**, 053406 (2017).
36. Liu, J. et al. Passive tumor targeting of renal-clearable luminescent gold nanoparticles: long tumor retention and fast normal tissue clearance. *J. Am. Chem. Soc.* **135**, 4978–4981 (2013).
37. Straus, W. Renal reabsorption and excretion of horseradish peroxidase. *Kidney Int.* **16**, 404–408 (1979).
38. Manning, M. C., Chou, D. K., Murphy, B. M., Payne, R. W. & Katayama, D. S. Stability of protein pharmaceuticals: an update. *Pharm. Res.* **27**, 544–575 (2010).
39. Kwong, G. A. et al. Mathematical framework for activity-based cancer biomarkers. *Proc. Natl Acad. Sci. USA* **112**, 12627–12632 (2015).
40. Yu, M. & Zheng, J. Clearance pathways and tumor targeting of imaging nanoparticles. *ACS Nano* **9**, 6655–6674 (2015).
41. Dai, Q. et al. Quantifying the ligand-coated nanoparticle delivery to cancer cells in solid tumors. *ACS Nano* **12**, 8423–8435 (2018).
42. Tang, S. et al. Tailoring renal clearance and tumor targeting of ultrasmall metal nanoparticles with particle density. *Angew. Chem. Int. Ed.* **55**, 16039–16043 (2016).
43. Wilhelm, S. et al. Analysis of nanoparticle delivery to tumours. *Nat. Rev. Mater.* **1**, 16014 (2016).
44. Von Maltzahn, G. et al. Nanoparticle self-assembly gated by logical proteolytic triggers. *J. Am. Chem. Soc.* **129**, 6064–6065 (2007).
45. Badeau, B. A., Comerford, M. P., Arakawa, C. K., Shadish, J. A. & Deforest, C. A. Engineered modular biomaterial logic gates for environmentally triggered therapeutic delivery. *Nat. Chem.* **10**, 251–258 (2018).

Acknowledgements

We thank H. Fleming (MIT) and A. Nogiwa-Valdez (Imperial) for critical reading and editing of the manuscript, M. Kumar (Bioimaging and Chemical Analysis Facilities, MIT) for help with the ICP–MS, M. Berne (Tufts University Core Facility) for peptide synthesis and K. Cormier and R. Bronson from the Koch Institute Histology Core. We acknowledge use of the characterization facilities at the Harvey Flower Electron Microscopy Suite (Department of Materials, Imperial College London) and the Light Microscopy Facilities at the Francis Crick Institute London. This study was supported in part by a Koch Institute Support Grant P30-CA14051 from the National Cancer Institute (Swanson Biotechnology Center), a Core Center Grant P30-ES002109 from the National Institute of Environmental Health Sciences, the Ludwig Fund for Cancer Research and the Koch Institute Marble Center for Cancer Nanomedicine. C.N.L., Q.C. and M.M.S. acknowledge generous support from the i-sense Engineering and Physical Sciences Research Council (EPSRC) IRC in Early Warning Sensing Systems for Infectious Diseases (EP/K031953/1; www.i-sense.org.uk). C.N.L. acknowledges support from the Marshall Aid Commemoration Commission. A.P.S. acknowledges support from the NIH Molecular Biophysics Training Grant and the National Science Foundation Graduate Research Fellowship. J.S.D. acknowledges support from the National Science Foundation Graduate Research Fellowship, the Ludwig Center for Molecular Oncology fellowship and the Siebel Scholar Foundation. A.N. acknowledges support from the Sir Henry Wellcome Postdoctoral Fellowship (209121_Z_17_Z) funding scheme from the Wellcome Trust. A.B. acknowledges support from the Early Postdoc Fellowship program (P2ELP2_178238) from the Swiss National Science Foundation. M.M.S., Y.L. and Q.C. acknowledge support from the European Research Council (ERC) Seventh Framework Programme Consolidator grant "Naturale CG" (616417). S.N.B. is a Howard Hughes Medical Institute Investigator.

Author contributions

C.N.L., A.P.S., J.S.D., S.N.B. and M.M.S. conceived and designed the research. C.N.L. and A.P.S. carried out all the experiments and analysed the data. Y.L. assisted with the peptide synthesis and characterization, A.N. performed the FCS measurements and analysis, A.B. assisted with the ICP–MS and Q.C. assisted with the TEM imaging. C.N.L., A.P.S., S.N.B. and M.M.S. wrote the manuscript with feedback from all the authors.

Competing interests

S.N.B., M.M.S., C.N.L. and A.P.S. have filed a patent application related to this research with the US Patent and Trademark Office. S.N.B. is a director at Vertex, co-founder and consultant at Glympse Bio, consultant for Cristal, Maverick and Moderna, and receives sponsored research funds from Johnson & Johnson.

Additional information

Supplementary information is available for this paper at https://doi.org/10.1038/s41565-019-0527-6.

Reprints and permissions information is available at www.nature.com/reprints.

Correspondence and requests for materials should be addressed to S.N.B. or M.M.S.

Peer review information: *Nature Nanotechnology* thanks Honggang Cui, Hui Wei and the other, anonymous, reviewer(s) for their contribution to the peer review of this work.

Publisher's note: Springer Nature remains neutral with regard to jurisdictional claims in published maps and institutional affiliations.

Methods

Materials. All the chemicals were purchased from Sigma-Aldrich unless otherwise stated. Milli-Q water (18.2 MΩ cm) was used in all the experiments.

AuNC synthesis. Synthesis and purification of peptide-capped AuNCs followed published procedures with the modifications outlined below[23]. We varied the ratio of the protease-cleavable peptide substrate to glutathione in the AuNC synthesis to incorporate functional handles onto the AuNC surface (P1:GSH or P2:GSH, tested at 1:2, 1:4, 1:5 and 1:9). Briefly, a freshly prepared aqueous solution of gold(III) chloride trihydrate ($HAuCl_4$, 20 mM, 100 µl) was mixed with 750 µl of deionized water in an Eppendorf tube, followed by the fast addition of L-glutathione reduced (GSH, 20 mM) and either peptide P1 or P2 (20 mM) so that final peptide content was fixed at a total volume of 150 µl in varying ratios of P1 or P2:GSH at 25 °C. The reaction mixture was heated to 70 °C under gentle stirring (500 r.p.m.) for 24 h. The reaction mixture changed from yellow to colourless within minutes and then turned pale yellow over ~12 h, which indicated the first reduction of Au(III) to Au(I) by the thiol group of the peptides, followed by the reduction of Au(I) thiolate complexes to Au(0) atoms over time assisted by the favourable reduction kinetics at the elevated reaction temperature[33,46]. After a 24 h synthesis, the resulting AuNC solution exhibited both orange luminescence and simultaneous peroxidase-like activity. The AuNCs could be stored at 4 °C for >6 months with negligible changes in optical or catalytic properties. The as-prepared AuNCs were purified through centrifugal ultrafiltration (Amicon Ultra centrifugal filter units Ultra-15, MWCO 10 kDa, Sigma) and buffer exchanged into PBS (pH 7.2). During ultrafiltration, the AuNCs were collected in the concentrate in the filter device, and any unbound peptide was collected in the filtrate. After purification, the AuNCs were resuspended in PBS (20 µM by AuNC particle concentration) and sterile filtered (Millex-GV Filter, Millipore, 0.22 µm).

The number of biotinylated ligands per AuNC was calculated by measuring the biotin concentration in the filtrate from the AuNC purification above, and subsequently subtracting this value from the starting concentration of biotinylated peptide used in the synthesis. The biotin concentration in the filtrate was quantified using the Pierce Biotin Quantitation kit in a 96-well plate following the manufacturer's instructions (Thermo Fisher) without any modifications. The molarity of the biotin in the sample was calculated using the extinction coefficient for HABA/avidin at 500 nm of 34,000 M^{-1} cm^{-1} and a path length of 0.5 cm.

Characterization of the nanoparticles. Dynamic light scattering (Zeta Sizer Nanoseries, Malvern Instruments, Ltd) was used to characterize the hydrodynamic diameter of the nanoparticles. Absorption measurements were recorded on a SpectraMax M5 multimode microplate reader (Molecular Devices, Ltd) using SoftMax Pro (Version 5.4) software. For the electron microscopy characterization, samples were drop cast onto carbon-coated copper grids (Electron Microscopy Sciences), and TEM imaging was performed using a JEOL 2100F operating at 200 kV. For the preparation of TEM samples, AuNC samples were first desalted (Zeba Spin Desalting Columns, 7K MWCO, Sigma) and 5 µl of the desalted sample was dropped onto the grid, allowed to incubate for 5 min and subsequently wicked with filter paper and dried overnight before imaging.

Evaluation of peroxidase-like activity. The colorimetric readout was carefully optimized to maximize the signal intensity from the AuNCs by varying the concentration of hydrogen peroxide, the pH and the concentration of sodium chloride, and measuring the corresponding catalytic activity under these conditions (Supplementary Fig. 6 and Supplementary Table 2). For the stability and catalytic activity of AuNCs in physiological environments, AuNCs (20 µM, 50 µl) were incubated with PBS (50 µl), synthetic urine (Surine Negative Urine Control, Sigma) or FBS (Gibco) for 1 h at 37 °C followed by a fivefold dilution in water. For the activity assay, 50 µl of each sample was added to a 96-well plate (Corning) followed by 150 µl of chromogenic substrate solution: 1-Step Ultra TMB ELISA Substrate Solution (Thermo Fisher) spiked to a final concentration of 4 M hydrogen peroxide (30% (w/w), Sigma). The A_{652} of the reaction solution was monitored for up to 25 min after the addition of substrate, which corresponds to the oxidation of TMB by H_2O_2.

For LoD assays, in a 96-well plate, synthetic urine (25 µl) was mixed with AuNCs (25 µl, varying concentrations, diluted in PBS), 5 M H_2O_2 (100 µl) and 1-Step Ultra TMB ELISA Substrate Solution (100 µl). A_{652} was measured every 20 s for 10 min, and linear regression was used to calculate the slope (A_{652} s^{-1}) over the first 150 s. The LoD was calculated as 3 s.d. above the mean background signal.

AuNC–NAv complex assembly. In a typical conjugation, 125 µl of NeutrAvidin Protein (NAv) (120 µM, PBS, Thermo Fisher) was mixed with 1 ml of AuNC–P1 or AuNC–P2 (20 µM) and incubated for 12 h with gentle shaking (500 r.p.m.) at 37 °C. Unbound AuNCs were removed from the AuNC–NAv complexes through centrifugal ultrafiltration (Amicon Ultra centrifugal filter units Ultra-15, MWCO 50 kDa, Sigma), where the AuNC–NAv complexes remained in the concentrate and any unbound AuNCs were collected in the filtrate. After ultrafiltration, the AuNC–NAv complexes were resuspended in PBS (30 µM by [AuNC]) and sterile filtered (Millex-GV Filter, Millipore, 0.22 µm).

In vivo renal clearance studies. All the animal studies were approved by the Massachusetts Institute of Technology (MIT) committee on animal care (MIT protocol 0417-025-20). All the animals received humane care, and all the experiments were conducted in compliance with institutional and national guidelines. GSH-templated and substrate-functionalized AuNCs were diluted to 10 µM AuNC in sterile PBS. Female Swiss Webster mice (4–6 weeks old, Taconic) were i.v. administered 2,000 pmol AuNCs via the tail vein (10 µM [AuNC], 200 µl). The injected dose of glutathione-templated AuNCs ranged from 1.6 to 2.4 mg kg^{-1} in terms of gold content, which is well below the maximal tolerated dose reported for both mice and non-human primates (1,059 mg kg^{-1} by GSH–AuNC content, ~530 mg kg^{-1} by gold content)[47].

After nanocluster injection, urine was collected at the indicated time points for catalytic activity assays and ICP–MS measurements. Mice were placed in custom housing with a 96-well plate base for urine collection. After 1 h, their bladders were voided and the collected urine volume measured. Clearance of the active AuNCs was quantified via a catalytic activity assay, and urine gold content was quantified by ICP–MS. The catalytic activity and gold content measurements of the collected urine samples were compared to those of the injected dose and normalized using urine volumes. Urine concentration may be dependent on many host and environmental factors, and therefore normalization between urine samples is required. In this study, we used the urine volume and injected dose for the normalization. Alternatively, co-administered free reporters that pass into urine independent of disease state, such as glutamate fibrinopeptide B[16] or inulin[48], could also be measured in urine and used to normalize the level of the AuNCs released by protease activity. Pearson's correlation coefficient (r) was computed to assess the relationship between renal clearance as measured by catalytic activity assay or ICP–MS (gold content).

Urine catalytic activity assays. For all the assays, 25 µl of urine was diluted into 25 µl of PBS in a transparent 96-well plate and allowed to equilibrate at room temperature for 15 min. Then, 100 µl each of 5 M H_2O_2 (Sigma) and TMB (Thermo Fisher) were added, and the plate was read kinetically at 652 nm over the course of 30 min. In all the catalytic activity assays that involved AuNCs in the collected urine, the final pH was acidic due to the acidic pH of the TMB and hydrogen peroxide substrate mix, which resulted in a final reaction pH < 4. For renal clearance studies, the concentration of the active AuNCs present in the urine was quantified via reference to a calibration curve of known AuNC concentrations. For the disease detection studies, the initial reaction velocity was quantified as the rate of change of A_{652} over the first 10 min of the reaction (A_{652} min^{-1}). Initial velocity analysis was preferred over the analysis of a single time-point measurement of absorbance at 652 nm, as urine collected from different mice had varying degrees of background levels of absorbance at this wavelength based on the hydration state of each mouse. This variable background was removed in the initial velocity analysis as the background absorbance from the initial coloration of urine was constant over time. The LoD was calculated to be the lowest concentration of the linear portion of the calibration curve (measured as the initial velocity of catalytic activity of the relevant AuNC batch).

ICP–MS on urine samples. Urine samples were digested in aqua regia (TraceMetal Grade hydrochloric acid, Fisher Chemical; ARISTAR ULTRA nitric acid, VWR) for 24 h. The digested samples were further diluted into an ICP–MS matrix composed of 4% HCl/4% HNO_3. The gold content in each sample was measured using an Agilent 7900 ICP–MS with an indium internal standard (5 ppb; TraceCERT, Sigma) and gold standard (Inorganic Ventures) for the calibration curve prepared in the ICP–MS matrix.

Cell culture. For the xenograft studies, LS174T (ATCC CL-188) cells were cultured in EMEM (ATCC) supplemented with 10% (v/v) FBS (Gibco) and 1% (v/v) penicillin–streptomycin (CellGro). For in vitro cytotoxicity assays, HEK293T (ATCC CRL-3216) cells were cultured in DMEM (ATCC) supplemented with 10% (v/v) FBS (Gibco) and 1% (v/v) penicillin–streptomycin (CellGro). Cells were passaged when confluence reached 80%.

In vitro cytotoxicity studies. For the in vitro cytotoxicity studies, HEK293T cells were plated in a 96-well plate (10,000 cells per well) and allowed to adhere to the wells. At 24 h post-seeding, the cells were incubated with varying concentrations of the AuNC–NAv complex (diluted in PBS) for 24 h. The cell viability was evaluated using the MTS (3-(4,5-dimethylthiazol-2-yl)-5-(3-carboxymethoxyphenyl)-2-(4-sulfophenyl)-2H-tetrazolium) assay (Promega).

In vivo toxicity studies. The AuNC–NAv complex (AuNC–$P1_{20}$–NAv or AuNC–$P2_{20}$–NAv, 15 µM [AuNC], 200 µl ≈ 3,000 pmol) was i.v. injected into immunocompetent female Swiss Webster mice (4–6 weeks old, Taconic). The mass of each mouse was monitored for 4 weeks p.i. and compared with masses of PBS-injected control mice. Heart, lung, liver, spleen and kidney tissues were collected from the mice at 1 h, 24 h or 10 days p.i., fixed in 10 wt% formalin, paraffin embedded, stained with haematoxylin and eosin and then examined by a veterinary pathologist and compared to organs from PBS-injected control mice.

Pharmacokinetic studies. To analyse the blood half-life of the AuNC–NAv complex, female Swiss Webster mice (4–6 weeks old, Taconic) were injected

with AuNC–$P2_{20}$–NAv (15 μM [AuNC], 200 μl ≈ 3,000 pmol) labelled with the photostable near-infrared dye Alexa Fluor 750 succinimidyl ester (Invitrogen). Blood was withdrawn retro-orbitally (~70 μl) and then immediately transferred into 70 μl of PBS with 5 mM EDTA and centrifuged to pellet blood cells. The concentration of the AuNC–NAv complex in plasma was measured using an Odyssey CLx infrared scanner (Li-Cor Inc.).

For biodistribution studies in healthy animals, female Swiss Webster mice (4–6 weeks old, Taconic) were injected with either near-infrared-dye-labelled AuNCs (10 μM [AuNC], 200 μl ≈ 2,000 pmol) or AuNC–$P2_{20}$–NAv complexes (15 μM [AuNC], 200 μl ≈ 3,000 pmol). Mice were sacrificed at 1 h, 3 h, 24 h, 1 week or 4 weeks p.i., and organ accumulations were measured using an Odyssey CLx scanner (Li-Cor Inc.) and quantified using ImageStudio (Version 5.2, Li-Cor Inc.). Organ accumulation was quantified as the signal intensity per unit area, calculated for each organ as the difference between the experimental group (AuNCs or AuNC–$P2_{20}$–NAv) versus the PBS-injected control. Values were scaled by a constant factor for all time points within each treatment group (near-infrared-dye-labelled AuNCs or AuNC–$P2_{20}$–NAv) to fall within the range shown. For mice injected with free AuNCs, the urine was also collected at the indicated time points and analysed by both ICP–MS (for the gold content analysis) and catalytic activity assay.

For biodistribution studies in tumour-bearing mice, nude mice that bore LS174T flank tumours were infused with either near-infrared-dye-labelled NAv carrier (VivoTag750, PerkinElmer; 1 μM by VT750), the MMP-cleavable AuNC–$P2_{20}$–NAv complex (15 μM [AuNC], 200 μl ≈ 3,000 pmol, Alexa Fluor 750) or free AuNCs (10 μM [AuNC], 200 μl ≈ 2,000 pmol, Alexa Fluor 750). Mice were sacrificed 1 h p.i., and organ and tumour accumulations were measured using an Odyssey CLx scanner (Li-Cor Inc.) and quantified using ImageStudio (Version 5.2, Li-Cor Inc.). Organ accumulation was quantified as the signal intensity per unit area, calculated for each organ as the difference between the experimental group (fluorescently labelled carrier, complex or free nanocluster) versus the PBS-injected control, and scaled to fall within the range shown.

Colorectal cancer xenograft studies. Female NCr Nude mice (4–5 weeks, Taconic) were injected bilaterally with 3×10^6 LS174T cells per flank. Two weeks after inoculation, tumour-bearing mice and age-matched controls were injected with either 15 μM MMP-sensitive or thrombin-sensitive (control) AuNC nanosensors in 200 μl of PBS (concentrations determined by [AuNC]). After the nanosensor injection, mice were placed in custom housing with a 96-well plate base for urine collection. Based on the measured blood half-life of the AuNC–NAv complex, the degree of tumour accumulation 1 h p.i., as well as our results from the FCS cleavage assays (80% of AuNCs cleaved from the complex within 1 h), we selected 1 h p.i. as our time point for urine collection[13,14,16]. After 1 h, bladders of the mice were voided to collect between 100 and 200 μl of urine. Urine was analysed via the catalytic activity measurements described above.

Statistical analyses. All the statistical analyses were conducted in GraphPad 7.0 (Prism). All the sample sizes and statistical tests are specified in the figure legends. The D'Agostino–Pearson test was used to assess normality and thus determine the statistical test used. For each animal experiment, groups were established before tumorigenesis or treatment with AuNC–PX, and therefore no randomization was used in the allocation of groups. Investigators were not blinded to the groups and treatments during the experiments.

Reporting summary. Further information on research design is available in the Nature Research Reporting Summary linked to this article.

Data availability

Research data is available online at https://doi.org/10.5281/zenodo.3256265.

References

46. Yu, Y., Luo, Z., Yu, Y., Lee, J. Y. & Xie, J. Observation of cluster size growth in CO-directed synthesis of $Au_{25}(SR)_{18}$ nanoclusters. *ACS Nano* **6**, 7920–7927 (2012).
47. Zheng, J. et al. Dose dependencies and biocompatibility of renal clearable gold nanoparticles. *Angew. Chem. Int. Ed.* **57**, 266–271 (2018).
48. Warren, A. D. et al. Disease detection by ultrasensitive quantification of microdosed synthetic urinary biomarkers. *J. Am. Chem. Soc.* **136**, 13709–13714 (2014).

nature research

Corresponding author(s): Sangeeta N. Bhatia & Molly M. Stevens

Last updated by author(s): July 2, 2019

Reporting Summary

Nature Research wishes to improve the reproducibility of the work that we publish. This form provides structure for consistency and transparency in reporting. For further information on Nature Research policies, see Authors & Referees and the Editorial Policy Checklist.

Statistics

For all statistical analyses, confirm that the following items are present in the figure legend, table legend, main text, or Methods section.

n/a	Confirmed
☐	☒ The exact sample size (*n*) for each experimental group/condition, given as a discrete number and unit of measurement
☐	☒ A statement on whether measurements were taken from distinct samples or whether the same sample was measured repeatedly
☐	☒ The statistical test(s) used AND whether they are one- or two-sided *Only common tests should be described solely by name; describe more complex techniques in the Methods section.*
☐	☒ A description of all covariates tested
☐	☒ A description of any assumptions or corrections, such as tests of normality and adjustment for multiple comparisons
☐	☒ A full description of the statistical parameters including central tendency (e.g. means) or other basic estimates (e.g. regression coefficient) AND variation (e.g. standard deviation) or associated estimates of uncertainty (e.g. confidence intervals)
☐	☒ For null hypothesis testing, the test statistic (e.g. *F*, *t*, *r*) with confidence intervals, effect sizes, degrees of freedom and *P* value noted *Give P values as exact values whenever suitable.*
☒	☐ For Bayesian analysis, information on the choice of priors and Markov chain Monte Carlo settings
☒	☐ For hierarchical and complex designs, identification of the appropriate level for tests and full reporting of outcomes
☐	☒ Estimates of effect sizes (e.g. Cohen's *d*, Pearson's *r*), indicating how they were calculated

Our web collection on statistics for biologists contains articles on many of the points above.

Software and code

Policy information about availability of computer code

Data collection	SoftMax Pro (Version 5.4) was used to collect data on SpectraMax M5 multimode microplate reader (Molecular Devices, Ltd.). Tecan i-control software (Version 3.7.3.0) was used to collect data on Tecan Infinite 200pro microplate reader (Tecan). ImageStudio (Version 5.2, Li-Cor Inc.) was used to collect data on Odyssey CLx imaging system (Li-Cor Inc.).
Data analysis	ZEN Software (Carl Zeiss, Jena, Germany) and PyCorrFit (Version 1.1.1) were used for FCS analysis (details in Methods). ImageStudio (Version 5.2, Li-Cor Inc.) was used for biodistribution image analysis, and ImageJ (NIH) was used for all other image analysis. Microsoft Excel (Version 16) and GraphPad Prism (Version 7.0) were used for all data analysis and statistics.

For manuscripts utilizing custom algorithms or software that are central to the research but not yet described in published literature, software must be made available to editors/reviewers. We strongly encourage code deposition in a community repository (e.g. GitHub). See the Nature Research guidelines for submitting code & software for further information.

Data

Policy information about availability of data

All manuscripts must include a data availability statement. This statement should provide the following information, where applicable:

- Accession codes, unique identifiers, or web links for publicly available datasets
- A list of figures that have associated raw data
- A description of any restrictions on data availability

The datasets from the study will be publicly available online at DOI: 10.5281/zenodo.3256265.

Field-specific reporting

Please select the one below that is the best fit for your research. If you are not sure, read the appropriate sections before making your selection.

☒ Life sciences ☐ Behavioural & social sciences ☐ Ecological, evolutionary & environmental sciences

For a reference copy of the document with all sections, see nature.com/documents/nr-reporting-summary-flat.pdf

Life sciences study design

All studies must disclose on these points even when the disclosure is negative.

Sample size	Sample size is indicated in the figure legend for each experiment. No sample-size calculations were performed. Sample size was determined to be adequate based on the magnitude and consistency of measurable differences between groups.
Data exclusions	No data was excluded for in vitro experiments. A pre-established exclusion criteria based on failed injection or insufficient urine volume collected for measurements was used for in vivo experiments; animals were excluded solely on the basis of these pre-established criteria.
Replication	All experiments were repeated independently at least three times with similar results.
Randomization	No randomization of mice; for tumour experiments, groups were established before tumourigenesis. All mice analyzed were sex- and age-matched.
Blinding	For histological analysis of toxicity, specimens were analyzed by a veterinary pathologist who was blinded to the treatment groups. In all other cases, investigators were not blinded to the groups and treatments during experiments. Data reported for these experiments are not subjective but based on the quantitative assays described.

Reporting for specific materials, systems and methods

We require information from authors about some types of materials, experimental systems and methods used in many studies. Here, indicate whether each material, system or method listed is relevant to your study. If you are not sure if a list item applies to your research, read the appropriate section before selecting a response.

Materials & experimental systems

n/a	Involved in the study
☒	☐ Antibodies
☐	☒ Eukaryotic cell lines
☒	☐ Palaeontology
☐	☒ Animals and other organisms
☒	☐ Human research participants
☒	☐ Clinical data

Methods

n/a	Involved in the study
☒	☐ ChIP-seq
☒	☐ Flow cytometry
☒	☐ MRI-based neuroimaging

Eukaryotic cell lines

Policy information about cell lines

Cell line source(s)	HEK293T cells, ATCC (CRL-3216); LS174T cells, ATCC (CL-188)
Authentication	Since these are commercially available cell lines, no further authentication was performed.
Mycoplasma contamination	All cell lines tested negative for mycoplasma contamination.
Commonly misidentified lines (See ICLAC register)	No commonly misidentified lines were used in the study.

Animals and other organisms

Policy information about studies involving animals; ARRIVE guidelines recommended for reporting animal research

Laboratory animals	All animal studies were approved by the Massachusetts Institute of Technology (MIT) committee on animal care (MIT protocol 0417-025-20). Female Swiss Webster mice (4-6 weeks, Taconic) were used for renal clearance, toxicity, and pharmacokinetic studies. Female NCR Nude mice (4-5 weeks at time of tumour induction, 6-7 weeks at time of urine test) were used for tumour studies. Complete descriptions can be found in relevant figure legends and Methods.

Wild animals	The study did not involve wild animals.
Field-collected samples	The study did not involve field-collected samples.
Ethics oversight	All animal studies were approved by the Massachusetts Institute of Technology (MIT) committee on animal care (MIT protocol 0417-025-20). All animals received humane care, and all experiments were conducted in compliance with institutional and national guidelines.

Note that full information on the approval of the study protocol must also be provided in the manuscript.